Journal of Power Sources 195 (2010) 7046–7053

Contents lists available at ScienceDirect

Journal of Power Sources

journal homepage: www.elsevier.com/locate/jpowsour

Fabrication of solid oxide fuel cell anode electrode by spray pyrolysis

Lin Liu, Gap-Yong Kim*, Abhijit Chandra

Iowa State University, Department of Mechanical Engineering, 2034 Black Engineering Building, Ames, IA 50011, USA

ARTICLE INFO

Article history:
Received 20 March 2010
Received in revised form 26 April 2010
Accepted 27 April 2010
Available online 11 May 2010

Keywords:
Solid oxide fuel cell
Spray pyrolysis
CGO
Anode

ABSTRACT

Large triple phase boundaries (TPBs) and high gas diffusion capability are critical in enhancing the performance of a solid oxide fuel cell (SOFC). In this study, ultrasonic spray pyrolysis has been investigated to assess its capability in controlling the anode microstructure. Deposition of porous anode film of nickel and $Ce_{0.9}Gd_{0.1}O_{1.95}$ on a dense 8 mol.% yttria stabilized zirconia (YSZ) substrate was carried out. First, an ultrasonic atomization model was utilized to predict the deposited particle size. The model accurately estimated the deposited particle size based on the feed solution condition. Second, effects of various process parameters, which included the precursor solution feed rate, precursor solution concentration and deposition temperature, on the TPB formation and porosity were investigated. The deposition temperature and precursor solution concentration were the most critical parameters that influenced the morphology, porosity and particle size of the anode electrode. Ultrasonic spray pyrolysis achieved homogeneous distribution of constitutive elements within the deposited particles and demonstrated capability to control the particle size and porosity in the range of 2–17 μm and 21–52%, respectively.

1. Introduction

Solid oxide fuel cells (SOFCs) are an electrochemical energy conversion device that can directly convert chemical fuel to electrical power with high efficiency and low emission of pollutants. One of the research efforts has been focusing on improving the performance of the SOFC electrodes [1–4]. The reactions in the electrodes occur at triple phase boundary (TPB) sites, where the reactant gas comes into contact with an electronic conductor and an ionic conductor [5]. Therefore, a SOFC electrode with greater TPBs provides more reaction sites, leading to an increase in electrical power output and better electrochemical performance. In the meanwhile, a highly porous electrode is required to efficiently supply fuel gas to the TPB sites. Therefore, designing and controlling the porous structure of an electrode is critical in improving the cell performance [6–8]. There have been efforts to improve the performance by introducing interface layers and making functionally graded electrodes. Nanocrystalline electrolyte–electrode interfacial layer has shown to increase the power output by more than 20% [9]. The functionally graded electrodes also showed better electrochemical performance than conventional SOFCs [10,11].

Various techniques have been investigated by scientists for the fabrication of electrodes, such as tape casting [12], screen printing [13], spin coating [14], tape calendaring [15], thermal plasma spraying [16], electrostatic spray deposition [17], and spray pyrolysis [18]. These techniques have been summarized and compared in Table 1 [19]. Spray pyrolysis is one of the most cost effective and versatile deposition techniques. It only requires a simple apparatus to deposit thin films of various materials under atmospheric condition. Compared with other techniques, spray pyrolysis has the capability to control particle shape, particle size, composition, and phase homogeneity of the deposited film. It has a great potential for producing functionally graded electrodes, which require deposition of multiple layers with gradually changing particle size, composition and/or porosity. Moreover, spray pyrolysis is compatible with large scale industry manufacturing for deposition of thin and porous films due to a wide selection of precursors and low equipment cost for mass production.

Several types of spray pyrolysis have been investigated to fabricate electrode layers in SOFCs. An electrostatic spray pyrolysis was used to make NiO-Samaria-doped ceria (SDC), YSZ and lanthanum strontium manganite (LSM) [17,20–22]. Porous electrode films of $La_{0.6}Sr_{0.4}Co_{0.2}Fe_{0.8}O_{3-\delta}$ [23] and Ni/CGO [24] have been fabricated by gas pressurized spray pyrolysis. An ultrasonic spray pyrolysis, which uses ultrasonic vibration to atomize the precursor solution, has been investigated to fabricate SOFC electrodes, as well. Hamedani et al. [25] fabricated a gradient porous LSM cathode, and Moe et al. [26] prepared $La_{1.8}Al_{0.2}O_3$ anode using ultrasonic spray pyrolysis. Chen et al. [18,27] deposited Ni–CGO anode by electrostatic-assisted ultrasonic spray pyrolysis to reduce the loss of aerosol stream to open air. However, none of the studies on ultrasonic spray pyrolysis investigated porosity of the deposited

* Corresponding author. Tel.: +1 515 294 6938; fax: +1 515 294 3261.
E-mail address: gykim@iastate.edu (G.-Y. Kim).

0378-7753/$ – see front matter © 2010 Elsevier B.V. All rights reserved.
doi:10.1016/j.jpowsour.2010.04.083

Table 1
Comparison of SOFC fabrication techniques [19].

Fabrication technique	Grading capability	Cost (time/complexity)	Porosity	Deposited film thickness
Tape casting	Poor	High	0–60	>7 μm
Screen printing	Poor	High	0–60	>8 μm
Spin coating	Yes	High	0–60	>1 μm
Tape calendaring	Poor	Low	N/A	N/A
Thermal plasma spray	Yes	Low	5–20	>Particle size
Electrostatic spray deposition	Yes	High	0–60	>Particle size
Spray pyrolysis	Yes	Medium	0–55	>Particle size

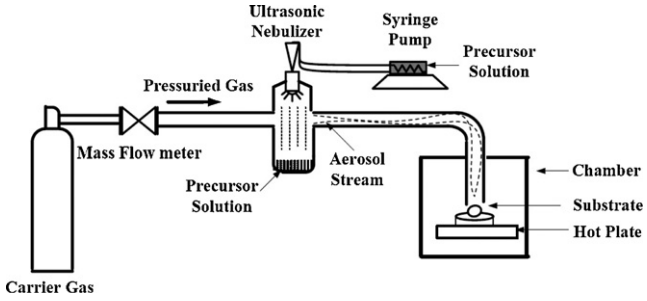

Fig. 1. Spray pyrolysis experiment setup.

electrode, which can influence the electrode performance [28]. Studies in applying spray pyrolysis for SOFC manufacturing are still very limited and further experiments accompanied by modeling are needed.

In this study, the ultrasonic spray pyrolysis was investigated for deposition of SOFC anode electrode to assess its capability to control the microstructure. A detailed experimental work was performed to deposit nickel and $Ce_{0.9}Gd_{0.1}O_{1.95}$ on an yttria stabilized zirconia (YSZ) substrate. First, an ultrasonic atomization model was utilized to predict the deposited particle size (Section 3). Second, the effects of various process parameters, which included deposition time (Section 4.1), precursor solution concentration (Section 4.2), deposition temperature (Section 4.3) and precursor solution feed rate (Section 4.4), on the microstructure and the porosity of deposited film were investigated. Among the parameters, precursor solution concentration and deposition temperature had the most significant effect on the microstructure.

Table 3
Values used to calculate deposition particle diameter (d_p) by ultrasonic atomization.

Precursor solution density (g ml^{-1})	0.88
Precursor solution surface tension (dynes cm^{-1})	20
Ultrasonic frequency (kHz)	60
Powder density, ρ_p (kg m^{-3})	775
Powder molecular mass, M_p (g mol^{-1})	348.85
Precursor solution molecular mass, M_{pr} (g mol^{-1})	71
Calculated average droplet diameter, d_d (μm)	100

2. Experimental procedures and materials

2.1. Experimental setup

The spray pyrolysis experimental setup is shown in Fig. 1. It consists of a carrier gas delivery system, a syringe pump, an ultrasonic nebulizer and a hot plate. The process can be divided into three main steps: atomization of precursor solution, transportation of the aerosol by the carrier gas, and deposition–decomposition of the precursor solution on the heated substrate. The system was designed to avoid deposition of large droplets formed by occasional variation of the ultrasonic nebulizer. It can effectively reduce the variation of atomized droplets, which will improve the uniformity of the deposited microstructures in the film. The precursor solution was atomized by ultrasonic nebulizer (Sonics® VC) operating at 60 kHz. The atomized aerosol was carried through a glass tube by the nitrogen (N_2) carrier gas at a flow rate (Q) of 1.5 l min^{-1}. The substrate was placed at the center of the hot plate. The distance between the tip of glass tube and substrate was fixed at 6 cm.

2.2. Materials and precursor solution preparation

In this study, 8 mol.% YSZ has been selected as the electrolyte material due to its wide use and affordability [29–31]. YSZ buttons (FCM®) were 20 mm in diameter and 270 μm in thickness. For

Table 2
Experimental matrix used in the study.

#	Precursor solution concentration (mol l^{-1})	Deposition temperature (°C)	Precursor solution feed rate (ml min^{-1})
1	0.4	250	1.23
2	0.4	300	1.23
3	0.4	350	1.23
4	0.1	250	1.23
5	0.1	300	1.23
6	0.1	350	1.23
7	0.025	250	1.23
8	0.025	300	1.23
9	0.025	350	1.23
10	0.4	250	1.78
11	0.4	300	1.78
12	0.4	350	1.78
13	0.1	250	1.78
14	0.1	300	1.78
15	0.1	350	1.78
16	0.025	250	1.78
17	0.025	300	1.78
18	0.025	350	1.78

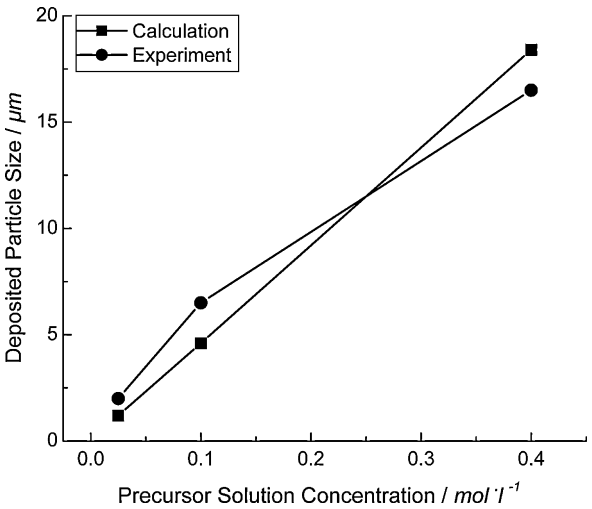

Fig. 2. Comparison of deposited particle size calculated from Eq. (4) and measured from experiments (L = 1.23 ml min^{-1}, Q = 1.5 l min^{-1}, T = 300 °C).

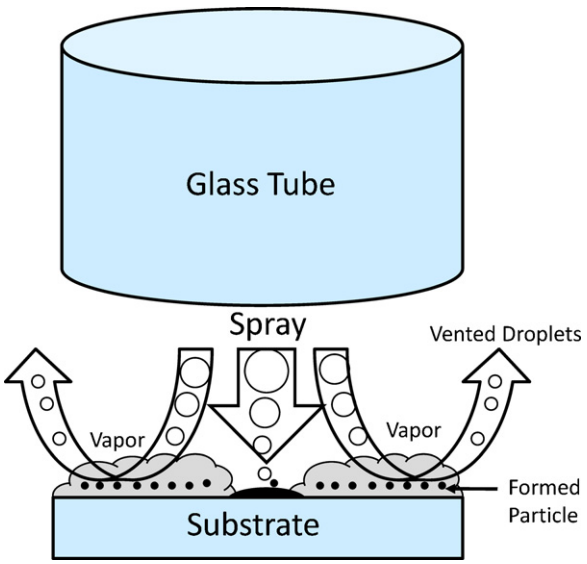

Fig. 3. The deposition mechanism of modified spray pyrolysis.

the anode material, Ni/CGO was selected. Ni/CGO ($Ce_{0.9}Gd_{0.1}O_{1.95}$) is considered one of the state-of-the-art anode materials due to its high ionic conductivity, high electronic conductivity and high thermal-chemical stability, particularly with YSZ electrolyte [20,32–39].

The precursor solution was prepared using a similar method proposed in [27]. Nickel(II) nitrate hexahydrate (98%, $N_2NiO_6{\cdot}6H_2O$; Alfa Aesar), cerium(III) nitrate hexahydrate (99.5%, $Ce(NO_3)_3{\cdot}6H_2O$; Alfa Aesar) and gadolinium(III) nitrate hydrate (99.9%, $Gd(NO_3)_3{\cdot}xH_2O$, $x \approx 6$; Alfa Aesar) were dissolved in the solution of diethylene glycol mono-n-butyl ether (99%, $HOCH_2CH_2OCH_2CH_2O(CH_2)_3CH_3$; Alfa Aesar) and ethyl alcohol (99.5%, C_2H_5OH; Decon) at a volume ratio of 1:1. The molar ratio

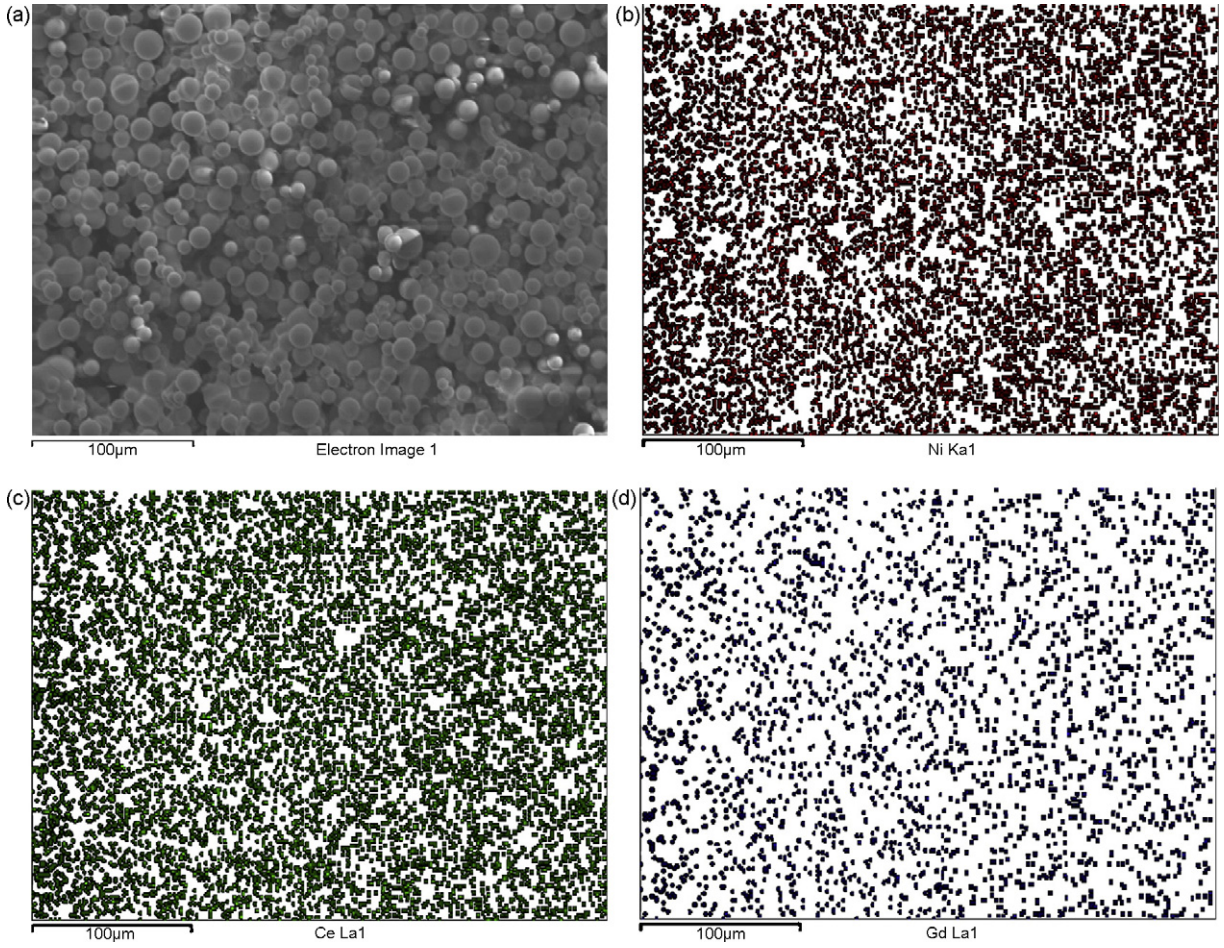

Fig. 4. EDS analysis of corresponding elements distribution. (a) SEM image of the analyzed area; (b) Ni; (c) Ce; (d) Gd.

Table 4
EDS data showing element composition in the deposited anode film.

Element	App conc.	Intensity corrn.	wt%	wt% sigma	at%
C	2.63	0.5533	4.75	0.41	14.38
O	31.82	1.2685	25.07	0.38	57.02
Ni	27.59	0.9434	29.22	0.37	18.11
Ce	33.39	0.9354	35.66	0.40	9.26
Gd	4.73	0.8923	5.30	0.33	1.23
Total			100.00		

of Ni to CGO was chosen as 6:4 based on the research conducted by Chen and Hwang [27], which resulted in the best performance in their study. Precursor solutions were prepared so that the total concentration of metal ions can be varied between 0.025 mol l^{-1} and 0.4 mol l^{-1}.

2.3. Anode film deposition and measurement

Three processing variables were investigated: precursor solution concentration (C), deposition temperature (T) and precursor solution feed rate (L). The full experiment matrix is summarized in Table 2. All the deposited samples were annealed at 800 °C for 2 h to promote crystallization of the deposited films at the heating and cooling rate of 5 °C min^{-1}. The morphology and composition of the deposited anode film were examined by scanning electron microscope (JEOL JSM-606LV) and energy dispersive X-ray spectrometer (INCA mics/x-stream/SEM TVA3). Images were analyzed by commercial software, ImageJ, to calculate the porosity values.

3. Ultrasonic atomization model

3.1. Modeling of deposited particle size

Understanding the relation among the ultrasonic atomization parameters can aid design and control of the deposited microstructure. However, only few studies have made efforts to model the deposited particle size in a SOFC. In this study, we employed the work by Jokanovic et al. [40,41]. The governing equation for ultrasonically atomized aerosol droplet in the ellipsoidal form is [42]:

$$\rho \frac{\partial^2 \phi}{\partial t^2}|_{r=R} - \frac{\sigma}{R^2}\left\{2\frac{\partial \phi}{\partial r} + \frac{\partial}{\partial r}\left[\frac{1}{\sin\theta}\frac{\partial(\sin\theta\frac{\partial\phi}{\partial\theta})}{\partial\theta} + \frac{1}{\sin^2\theta}\frac{\partial^2\phi}{\partial\varepsilon^2}\right]\right\} = 0 \quad (1)$$

where ϕ is the rate potential of excitation precursor; r is radius of the aerosol droplet; and ε and θ are angles corresponding to the equation transformed into polar coordinates. The solution of Eq. (1) can be obtained in the following form [42]:

$$\rho\omega^2 + \frac{l\sigma}{R^3}[2 - l(l+1)] = 0 \quad (2)$$

where ω is the spherical frequency of ultrasonic wave oscillation. The average diameter of an aerosol droplet (d_d) is obtained by solving Eq. (2) [42],

$$d_d = 2\frac{\sqrt[3]{2}}{\pi}\left(\frac{\pi\sigma}{\rho f^2}\right)^{1/3} \quad (3)$$

where σ is the surface tension of the precursor solution, ρ is the precursor solution density, and f is the frequency of the ultrasonic nebulizer.

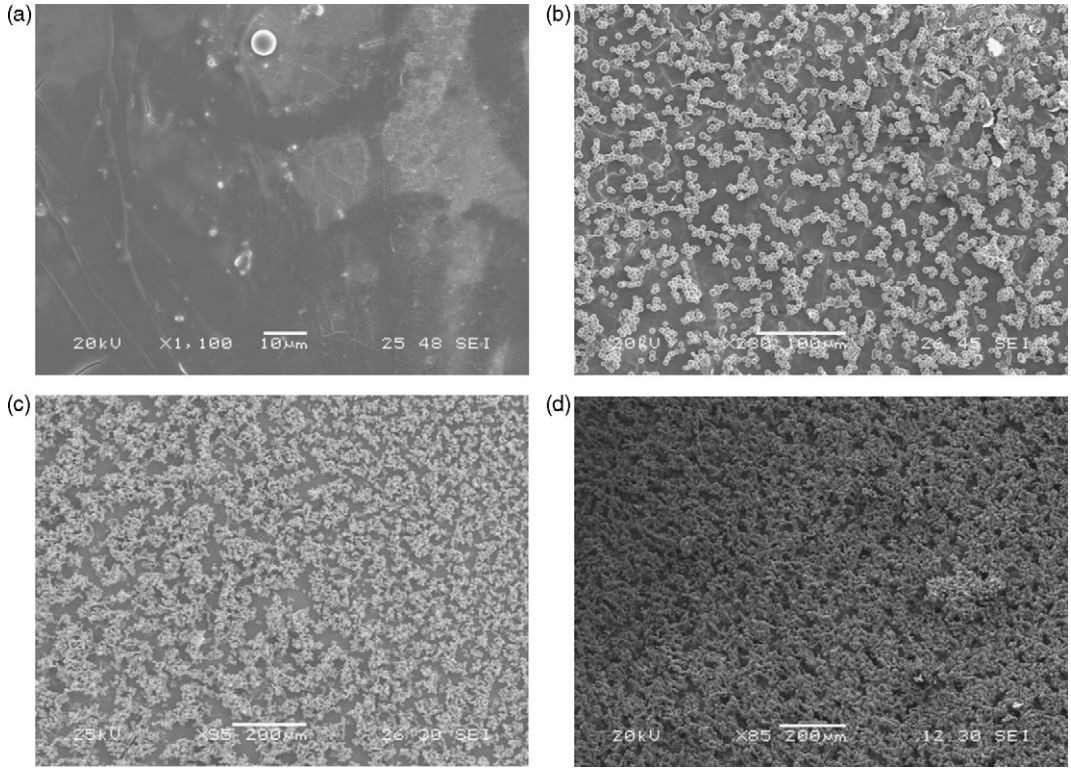

Fig. 5. Deposited substrate morphology at different deposition times (L = 1.23 ml min^{-1}, Q = 1.5 l min^{-1}, C = 0.1 mol l^{-1}, T = 300 °C). (a) After 15 min; (b) after 30 min; (c) after 45 min; (d) after 120 min.

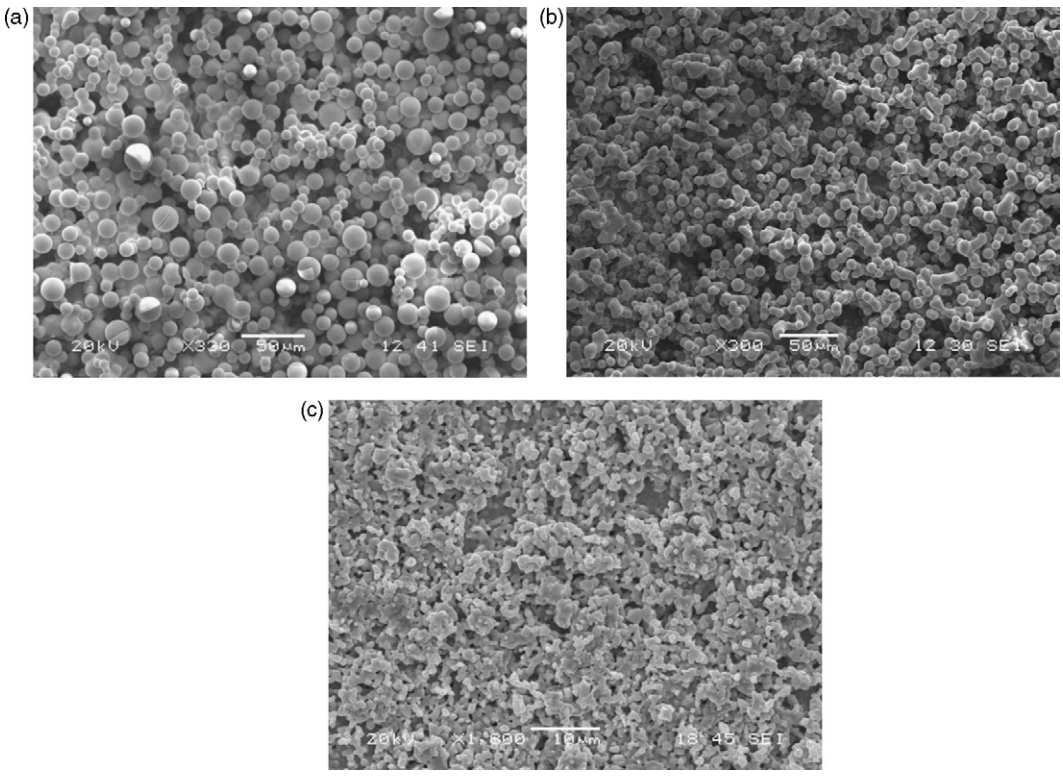

Fig. 6. Images of deposited anode film at different precursor solution concentrations (L = 1.23 ml min^{-1}, Q = 1.5 l min^{-1}, T = 300 °C). (a) C = 0.4 mol l^{-1}; (b) C = 0.1 mol l^{-1}; (c) C = 0.025 mol l^{-1}.

The diameter of discharged aerosol droplet from the nebulizer decreases during the solidification and pyrolysis steps. The eventual deposited particle diameter (d_p) can be expressed by the following formula [42]:

$$d_p = d_d \left(\frac{c_{pr} M_p}{\rho_p M_{pr}} \right)^{1/3} \quad (4)$$

where c_{pr} is the precursor solution concentration, M_p is the powder molecular mass, ρ_p is the powder density, and M_{pr} is the molecular mass of the precursor solution.

3.2. Model validation

The surface tension of the precursor solution was calculated based on the volume fraction of the ethyl alcohol and butyl ether without considering the influence of other element concentrations [43]. The surface tensions of ethyl alcohol and butyl ether are 22.32 and 17.06 dynes cm^{-1}, respectively. Therefore, the surface tension of the precursor solution was assumed to be 20.0 dynes cm^{-1} considering 1:1 volume mixing. Eqs. (3) and (4) were used to calculate the average diameter of an aerosol droplet and deposited particle diameters. Parameters used in the calculation are summarized in Table 3. The calculated deposited particle size and experimentally measured values have a good agreement as shown in Fig. 2. Changing the concentration of precursor solution does not influence the aerosol droplet size, but the concentration of the precursor solution determines the eventual particle size deposited. Capability to predict the deposited particle size will help to control and design the anode microstructure.

4. Results and discussion

The ultrasonic spray pyrolysis setup used in this study has the characteristics of conventional spray pyrolysis and chemical vapor deposition (CVD). The deposition mechanism of the ultrasonic spray pyrolysis used in this study is schematically described in Fig. 3. In conventional spray pyrolysis, the deposition solely occurs from high-velocity particles that strike the surface. In this approach, precursor aerosol is transported by a carrier gas that enables deposition by evaporation–decomposition of precursor solution droplets. Therefore, the anode film is formed and thickened by the accumulation of droplets similar to that of liquid delivery of CVD [25,44,45].

4.1. Analysis of the deposited anode film microstructure

In this section, the composition and microstructure evolution of the deposited anode film are analyzed. The compositional anal-

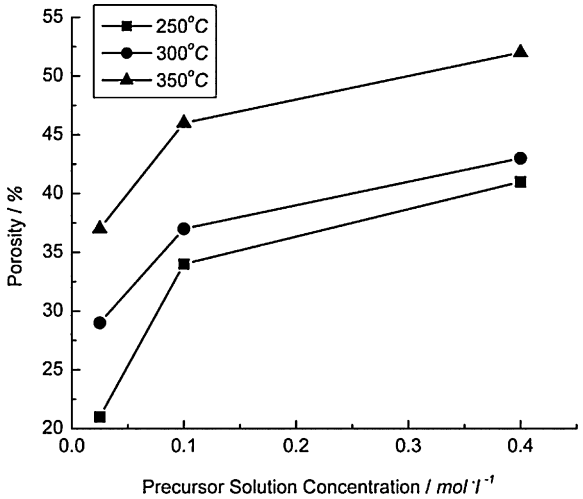

Fig. 7. Effect of temperature and precursor solution concentration on deposited anode film porosity (L = 1.23 ml min^{-1}, Q = 1.5 l min^{-1}).

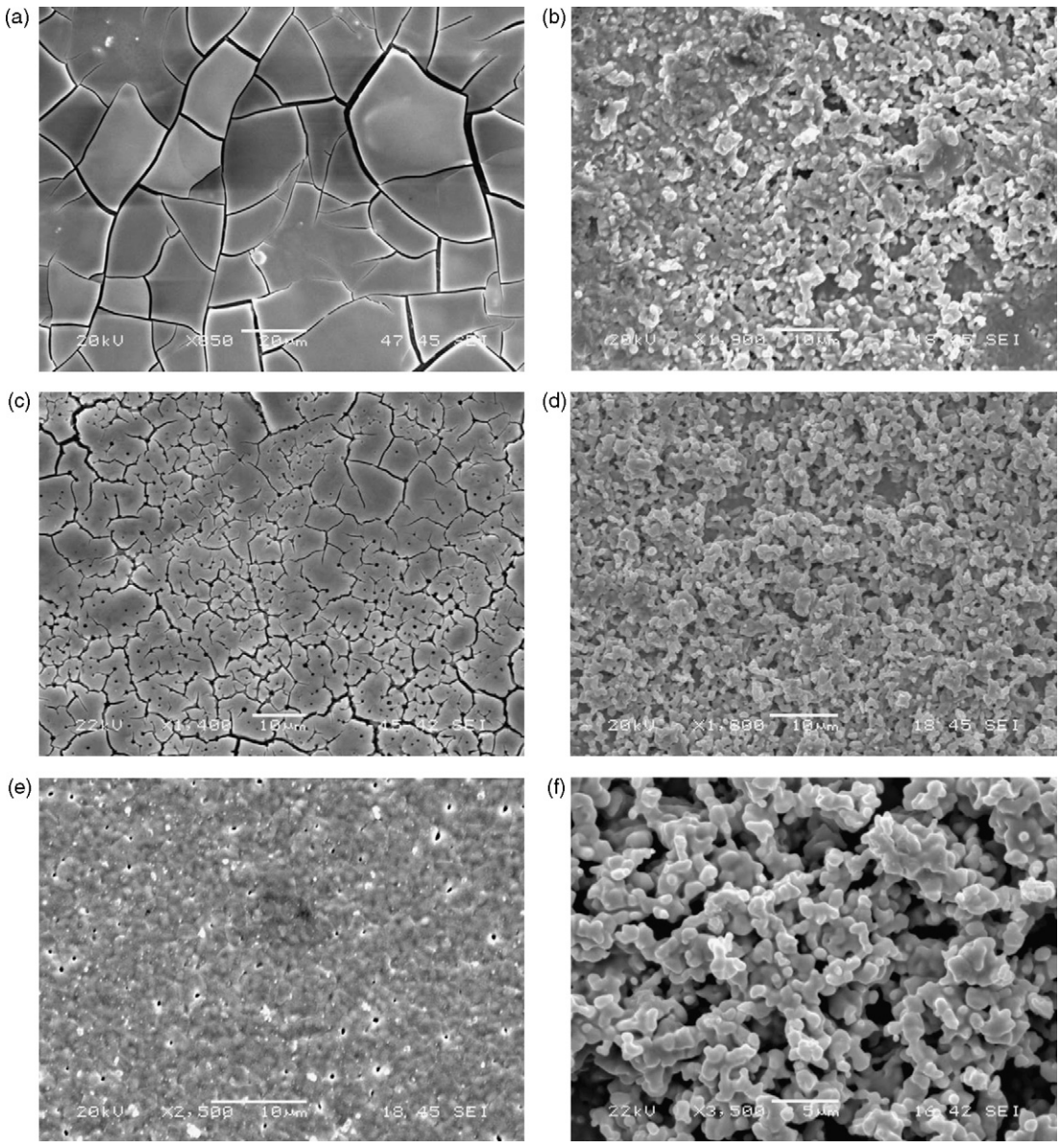

Fig. 8. Images of deposited anode film at various deposition temperatures (L = 1.23 ml min^{-1}, Q = 1.5 l min^{-1}, C = 0.025 mol l^{-1}). (a) T = 250 °C bottom layer; (b) T = 250 °C top layer; (c) T = 300 °C bottom layer; (d) T = 300 °C top layer; (e) T = 350 °C bottom layer; (f) T = 350 °C top layer.

ysis of a typical anode film by EDS is summarized in Table 4. The measured composition ratio of Ni/Ce/Gd was 15:8:1 as presented in Table 4. This is close to the theoretically calculated value of 15:9:1 based on the molar of ratio of Ni and CGO, which was 6:4. The weight ratio of NiO and CGO is about 50:50 without considering carbon, which comes from the decomposition of the precursor solution. In addition, the deposited anode film was analyzed by EDS mapping technique to reveal the element distribution of Ni, Ce and Gd. As evident in Fig. 4, the elements are homogenously distributed in the deposited film and within each particle. The proposed method is capable of fabricating anode composite film with well-dispersed constitutive elements.

As the deposition time progresses, the deposited film morphologies evolve as shown in Fig. 5. After 15 min, highly crystallized, dense deposition film was observed (see Fig. 5(a)). The porosity of the deposition film also increased, which agreed with prior work performed by Nguyen and Djurado [17]. The initial dense deposition layer can be classified as type II morphology categorized by Schoonman and co-workers [46]. Rapid spreading of the precursor solution droplet may be the reason for the formation of a dense layer [17]. Once the deposition time passed 30 min, the deposited particles agglomerated and a columnar structure formed as shown in Fig. 5(c). Due to evolving microstructures during the deposition process, the deposition rate increased from 0.10 μm min^{-1} to 0.24 μm min^{-1} after 60 min of deposition time. When the deposition time reached 60 min, a porous top layer was formed on the dense bottom layer in accordance with the type III morphology [46].

4.2. Effect of precursor solution concentration

Effects of precursor solution concentration on deposited particle size and porosity were analyzed. As shown in Fig. 6, higher precursor solution concentration resulted in deposition of larger particles. The particle size increased from 2 μm to 20 μm when the precursor solution concentration increased from 0.025 mol l^{-1} to 0.4 mol l^{-1}. Therefore, by lowering the precursor solution concentration, particles with sub-micrometer size can be deposited. As the solution

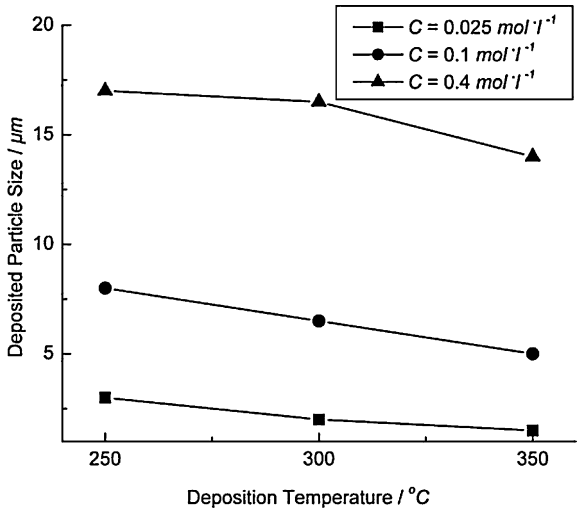

Fig. 9. Effect of temperature and precursor solution concentration on deposited particle size ($L = 1.23\ \mathrm{ml\ min^{-1}}$, $Q = 1.5\ \mathrm{l\ min^{-1}}$).

concentration increased, higher porosity was obtained due to the formation of large particles with a high degree of agglomeration (see Fig. 7). The porosity increased from 21% to 38% by changing the precursor solution concentration from 0.025 mol $\mathrm{l^{-1}}$ to 0.4 mol $\mathrm{l^{-1}}$ when the deposition temperature was 250 °C. While the precursor concentration should not exceed the solubility limit of the chemical compounds, it should not be too low to achieve a reasonable deposition rate. At low concentration, the particles will be blown away from the substrate by the carrier gas, and therefore, the deposition rate will be very low. The precipitated particle needs to be above a minimum size in order to overcome the thermophoresis force.

4.3. Effect of deposition temperature

The deposition temperature also significantly influenced the morphology and porosity of the microstructure. A relatively dense layer is formed in the beginning of deposition near the YSZ interface and is referred to as bottom layer. A porous film formed and accumulated on top of the bottom layer. As shown in Fig. 8, the bottom layer (YSZ interface) and the top layer (the free surface) showed distinctly different structures at three temperatures. Fewer cracks were found at higher temperature in the bottom layer. The deposition temperature at least should be above the boiling temperature of the precursor solution, which will guarantee an effective evaporation of the solution during deposition of the atomized droplet. Low deposition temperatures below 250 °C is not appropriate for anode film deposition because the droplets cannot be easily vaporized due to the high boiling temperature of diethylene glycol mono-n-butyl ether. Even at 250 °C, the excessive amount of precursor solution remains on the substrate for too long and results in surface cracks as shown in Fig. 8(a). Similar results were reported by Wilhelm et al. [21].

The higher deposition temperature resulted in higher porosity in the deposited film as shown in Fig. 7. The large amount of vapor generated from the fast evaporating solvent during high deposition temperature is assumed to be responsible for the high porosity of the deposited film [47]. On the other hand, the diameter of atomized droplet decreased as it decomposed into smaller particles at higher deposition temperatures (see Fig. 9). However, temperatures above 450 °C should be avoided because the deposited film can break and result in numerous cracks and serious delamination due to the high thermal stress, as shown in Fig. 10. Similar phenomena were reported by Bohac and Gauckler [47]. Extremely high deposition temperature causes complete evaporation of the atomized droplet, and the precipitated particles are blown away before they can reach the substrate. Consequently, the deposition rate decreases significantly.

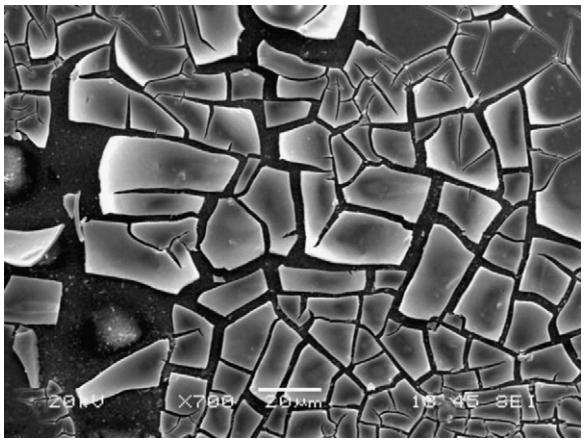

Fig. 10. Severely cracked deposited anode film near the YSZ interface (bottom layer) ($L = 1.23\ \mathrm{ml\ min^{-1}}$, $Q = 1.5\ \mathrm{l\ min^{-1}}$, $C = 0.1\ \mathrm{mol\ l^{-1}}$, $T = 450$ °C).

4.4. Effect of precursor solution feed rate

Precursor solution feed rate did not influence the deposited anode film microstructure and morphology as significantly as the precursor solution concentration or the deposition temperature. The precursor solution feed rate determines the amount of atom-

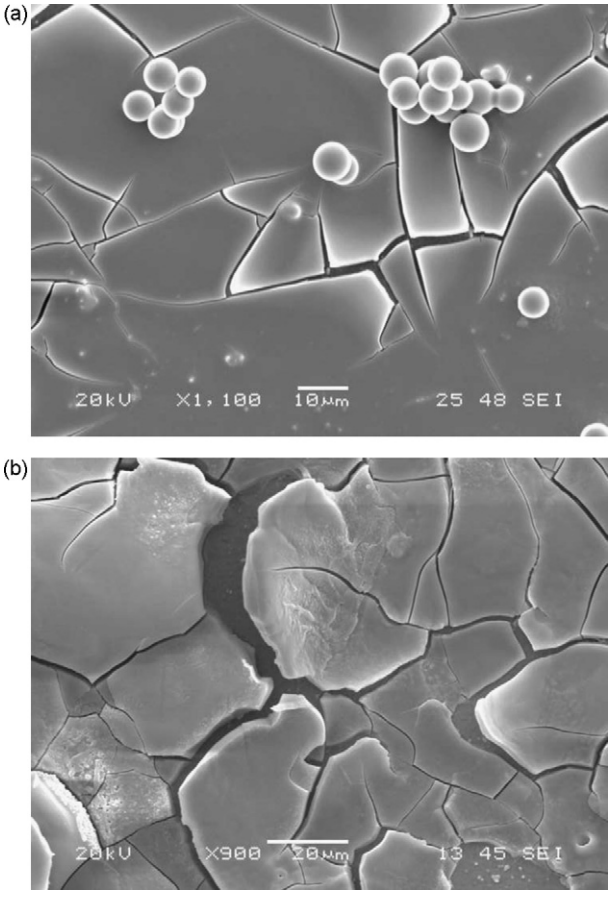

Fig. 11. Images of deposited anode film near the YSZ interface (bottom layer) at different precursor solution feed rate ($Q = 1.5\ \mathrm{l\ min^{-1}}$, $C = 0.1\ \mathrm{mol\ l^{-1}}$, $T = 250$ °C). (a) $L = 1.23\ \mathrm{ml\ min^{-1}}$; (b) $L = 1.78\ \mathrm{ml\ min^{-1}}$.

ized precursor solution reaching the substrate. At higher solution feed rate, larger amount of droplets reach the substrate. Increase of precursor solution on the substrate requires longer decomposition and drying time. This leads to denser layer and more severe cracks. The deposited bottom layer morphologies are shown in Fig. 11. When the precursor solution feed rate increased from 1.23 ml min^{-1} to 1.7 ml min^{-1}, the porosity of the film and the diameter of the deposited particle remained relatively constant at 37% and 7.5 μm, respectively. The precursor solution feed rate only had minimal influence on the deposited anode film microstructure and morphology.

5. Conclusion

An ultrasonic spray pyrolysis technique was investigated to deposit Ni–CGO anode electrode of an SOFC to assess its capability to control the deposited microstructure. The effects of processing parameters, including deposition time, precursor solution concentration, deposition temperature and precursor solution feed rate, on the deposited anode film morphology and porosity were analyzed. Following conclusions may be drawn from this study:

(i) The ultrasonic spray pyrolysis demonstrated its capability to uniformly disperse the constitutive elements. The EDS analysis showed that all the elements were homogenously distributed on the substrate and within each particle.
(ii) The ultrasonic atomization model based on Jokanovic et al. [40,41] was capable of accurately predicting the size of deposited anode particle. The model can be a useful tool to design and deposit optimal microstructure.
(iii) The precursor solution concentration and deposition temperature were the most critical parameters that influenced the morphology and porosity of the deposited microstructure. The deposition temperature influenced the integrity of the deposited layer and deposition rate.
(iv) The study finds that by controlling these parameters, deposition particle size in the range of 2–17 μm and porosity in the range of 22–54% can be controlled by ultrasonic spray pyrolysis for Ni–CGO anode.

The study demonstrated the potential of ultrasonic spray pyrolysis for tailoring the microstructure of the anode electrode of a SOFC. AC impedance and DC electrical conductivity tests are planned in near future to understand the relationship between the electrode microstructure and cell performance. Eventually, the relation between the electrochemical and thermomechanical properties of the electrode film needs to be understood for optimal electrode design.

References

[1] S.P. Jiang, W. Wang, Y.D. Zhen, J. Power Sources 147 (2005) 1–7.
[2] S.P. Yoon, S.W. Nam, J. Han, T.H. Lim, S.A. Hong, S.H. Hyun, Solid State Ionics 166 (2004) 1–11.
[3] A. Ali, X. Wen, K. Nandakumar, J. Luo, K.T. Chuang, J. Power Sources 185 (2008) 961–966.
[4] H. Uchida, S. Arisaka, M. Watanabe, Solid State Ionics 135 (2000) 347–351.
[5] R. O'Hayre, D.M. Barnett, F.B. Prinz, J. Electrochem. Soc. 152 (2005) A439–A444.
[6] C.W. Tanner, K.Z. Fung, A.V. Virkar, J. Electrochem. Soc. 144 (1997) 21–30.
[7] J. Deseure, Y. Bultel, L. Dessemond, E. Siebert, Electrochim. Acta 50 (2005) 2037–2046.
[8] E.S. Greene, W.K.S. Chiu, M.G. Medeiros, J. Power Sources 161 (2006) 225–231.
[9] A.O. Stoermer, J.L.M. Rupp, L.J. Gauckler, Solid State Ionics 177 (2006) 2075–2079.
[10] J. Will, A. Mitterdorfer, C. Kleinlogel, D. Perednis, L.J. Gauckler, Solid State Ionics 131 (2000) 79–96.
[11] K. Jono, S. Suda, M. Hattori, ECS Trans. 7 (2007) 1541–1546.
[12] J.H. Song, S.I. Park, J.H. Lee, H.S. Kim, J. Mater. Process. Technol. 198 (2008) 414–418.
[13] D. Rotureau, J.P. Viricelle, C. Pijolat, N. Caillol, M. Pijolat, J. Eur. Ceram. Soc. 25 (2005) 2633–2636.
[14] X. Xu, C. Xia, S. Huang, D. Peng, Ceram. Int. 31 (2005) 1061–1064.
[15] N.Q. Minh, Solid State Ionics 174 (2004) 271–277.
[16] R. Hui, Z.W. Wang, O. Kesler, L. Rose, J. Jankovic, S. Yick, R. Maric, D. Ghosh, J. Power Sources 170 (2007) 308–323.
[17] T. Nguyen, E. Djurado, Solid State Ionics 138 (2001) 191–197.
[18] C.-L. Chang, C.-S. Hsu, B.-H. Hwang, J. Power Sources 179 (2008) 734–738.
[19] R.R. Flesner, Mechanical Engineering, Iowa State University, Ames, 2009, pp. 28–29.
[20] Y. Xie, R. Neagu, C.-S. Hsu, X. Zhang, C. Deces-Petit, ECS Trans. 7 (2007) 787–794.
[21] O. Wilhelm, S.E. Pratsinis, D. Perednis, L.J. Gauckler, Thin Solid Films 479 (2005) 121–129.
[22] A. Princivalle, D. Perednis, R. Neagu, E. Djurado, Chem. Mater. 16 (2004) 3733–3739.
[23] D. Beckel, A. Dubach, A. Studart, L. Gauckler, J. Electroceram. 16 (2006) 221–228.
[24] U.P. Muecke, G.L. Messing, L.J. Gauckler, Thin Solid Films 517 (2009) 1515–1521.
[25] H.A. Hamedani, K.-H. Dahmen, D. Li, H. Peydaye-Saheli, H. Garmestani, M. Khaleel, Mater. Sci. Eng.: B 153 (2008) 1–9.
[26] K.K. Moe, T. Tagawa, S. Goto, Preparation of Electrode Catalyst for SOFC Reactor by Ultrasonic Mist Pyrolysis: Effect of Spray Time, Nippon Seramikkusu Kyokai, Tokyo, Japan, 1998.
[27] J.C. Chen, B.H. Hwang, J. Am. Ceram. Soc. 91 (2008) 97–102.
[28] F. Zhao, A.V. Virkar, J. Power Sources 141 (2005) 79–95.
[29] K. Prabhakaran, M.O. Beigh, J. Lakra, N.M. Gokhale, S.C. Sharma, J. Mater. Process. Technol. 189 (2007) 178–181.
[30] H. Zhao, X. Li, F. Ju, U. Pal, J. Mater. Process. Technol. 200 (2008) 199–204.
[31] D. Simwonis, H. Thülen, F.J. Dias, A. Naoumidis, D. Stöver, J. Mater. Process. Technol. 92–93 (1999) 107–111.
[32] K. Chen, L. Zhe, N. Ai, X. Chen, J. Hu, X. Huang, W. Su, J. Power Sources 167 (2007) 84–89.
[33] J. Van herle, R. Ihringer, R. Vasquez Cavieres, L. Constantin, O. Bucheli, J. Eur. Ceram. Soc. 21 (2001) 1855–1859.
[34] M.G. Chourashiya, S.H. Pawar, L.D. Jadhav, Appl. Surf. Sci. 254 (2008) 3431–3435.
[35] M. Shi, N. Liu, Y.D. Xu, C. Wang, Y.P. Yuan, P. Majewski, F. Aldinger, J. Mater. Process. Technol. 169 (2005) 179–183.
[36] B.C.H. Steele, Solid State Ionics 129 (2000) 95–110.
[37] V.V. Kharton, F.M. Figueiredo, L. Navarro, E.N. Naumovich, A.V. Kovalevsky, A.A. Yaremchenko, A.P. Viskup, A. Carneiro, F.M.B. Marques, J.R. Frade, J. Mater. Sci. 36 (2001) 1105–1117.
[38] K. Higashinakagawa, S. Sameshima, Y. Hirata, J. Ceram. Process. Res. 5 (2004) 84–88.
[39] S. Suda, M. Itagaki, E. Node, S. Takahashi, M. Kawano, H. Yoshida, T. Inagaki, J. Eur. Ceram. Soc. 26 (2006) 593–597.
[40] V. Jokanović, Mater. Trans., JIM 37 (1996) 627.
[41] V. Jokanović, A.M. Spasić, D. Uskoković, J. Colloid Interface Sci. 278 (2004) 342–352.
[42] V. Jokanovic, D. Janackovic, D. Uskokovic, Ultrason. Sonochem. 6 (1999) 157–169.
[43] C.Y. Chen, T.K. Tseng, C.Y. Tsay, C.K. Lin, J. Mater. Eng. Perform. 17 (2008) 20–24.
[44] D. Perednis, L.J. Gauckler, J. Electroceram. 14 (2005) 103–111.
[45] K.L. Choy, B. Su, Thin Solid Films 388 (2001) 9–14.
[46] N.H.J. Stelzer, C.H. Chen, L.N. van Rij, J. Schoonman, in: A.J.M.a.K. Nisancioglu (Ed.), Materials and Processes10th I.E.A. SOFC Workshop, Switzerland, 1997, 236 pp.
[47] P. Bohac, L. Gauckler, Solid State Ionics 119 (1999) 317–321.